PROCEEDINGS A

royalsocietypublishing.org/journal/rspa

Research

Cite this article: Huang W, Liu Z, Liu M, Hsia KJ. 2024 Snap-through eversion of axisymmetric shells under contact indentation. *Proc. R. Soc. A* **480**: 20240303.
https://doi.org/10.1098/rspa.2024.0303

Received: 23 April 2024
Accepted: 11 September 2024

Subject Category:
Engineering

Subject Areas:
mechanics, mechanical engineering

Keywords:
axisymmetric shell, snap-through, contact mechanics, eversion, geometric nonlinearity, discrete model

Authors for correspondence:
Mingchao Liu
e-mail: m.liu.2@bham.ac.uk
Weicheng Huang
e-mail: weicheng.huang@newcastle.ac.uk
Zhaowei Liu
e-mail: zhaowei.liu@hhu.edu.cn
K. Jimmy Hsia
e-mail: kjhsia@ntu.edu.sg

THE ROYAL SOCIETY PUBLISHING

Snap-through eversion of axisymmetric shells under contact indentation

Weicheng Huang[1], Zhaowei Liu[2], Mingchao Liu[3] and K. Jimmy Hsia[4,5]

[1]School of Engineering, Newcastle University, Newcastle upon Tyne NE1 7RU, UK
[2]College of Mechanics and Engineering Science, Hohai University, Nanjing 211000, People's Republic of China
[3]Department of Mechanical Engineering, University of Birmingham, Birmingham B15 2TT, UK
[4]School of Mechanical and Aerospace Engineering, Nanyang Technological University, Singapore 639798, Singapore
[5]School of Chemistry, Chemical Engineering and Biotechnology, Nanyang Technological University, Singapore 639798, Singapore

ML, 0000-0001-7424-4794

In this paper, we systematically investigate the stability of an axisymmetric shell and the snap-through eversion induced by indentation through a discrete numerical approach. To capture the intricate interplay between the geometric and boundary nonlinearities during contact actuation, we employ the discrete axisymmetric shell model accompanied by the incremental potential formulation for our analysis. Our results reveal that the indentation response of a spherical shell can be classified into three groups, i.e. monotonous, monostable and bistable behaviours, whose boundaries can be characterized by a simple scaling law. We further discover that, for bistable shells, the snap-through eversion happens at a critical state where the configurations are universal, which is independent of the indenter size and can be captured by a simple geometric model. One interesting prediction of our model is that, with increasing indenter size, the contact state between the shell and indenter changes from conformal contact to partial separation, which is validated by a finite element method simulation. Our findings may provide explanations for some biophysical phenomena (e.g. cell fusion) and can also guide optimal designs of intelligent structures (e.g. soft actuators and soft robots).

1. Introduction

Axisymmetric shell structures are prevalent in many areas, ranging from fruit skins and biological vesicles in nature, to engineered structures such as submarines, biomedical devices and space capsules [1]. Study of their mechanical behaviours is essential for their applications [2]. Especially, predicting the ways these shells deform and fail under various loading is key to ensuring their intended functionalities and safety.

The stability of shell structures has been a significant focus for many decades due to its critical importance across a broad spectrum of engineering applications. This importance is particularly noted in shell design and construction [3]. Based on their stability, shell structures exhibit varying mechanical behaviours and offer potential for diverse applications. For instance, bistable shells have been utilized to develop innovative structures with new functionalities [4,5], such as nonlinear mechanical responses [6], shape-morphing [7,8] and pattern formation [9,10]. Specifically, a key phenomenon in bistable shells is snap-through (or 'snapping') instability, that is the sudden transition from one equilibrium state to another [3]. This instability occurs in various scenarios, including, e.g. during the abrupt closure of Venus flytrap leaves [11] and pneumatic-actuated soft jumping robots [12]. Snap-through of shells can be triggered through different stimuli, including indentation [13–16], pressure [9,10,12], magnetic actuation [17,18], chemical diffusion [19], strain mismatch [20] and mechanical contact [21], etc. In recent years, there has been growing interest in exploring snap-through instabilities due to their significant potential for applications such as robotic actuation [12,22].

Despite the distinct advantages offered by shell snapping, its underlying mechanisms remain largely unexplored, particularly in scenarios involving geometric and boundary nonlinearities. Over the past decades, the critical conditions for buckling have been delineated through shell theory [23–26], including instances with geometric imperfections [24,27–29]. Furthermore, the rate-dependent buckling behaviours of viscoelastic shells have also been examined [30–33]. However, most shell theories rely on the premises of small strain and moderate rotation [34], assumptions that are invalid in cases of shell snapping or eversion, where large strain and rotation are present as the shells turn inside-out. Additionally, directly solving the ordinary differential equations (ODEs) of shell theory through functional variation proves to be complex or even unfeasible, particularly when the shell faces intricate loading conditions such as nonlinear contact indentation. While the finite element method (FEM) can accommodate large deformations and finite rotations with its geometrically nonlinear formulation [3,6,12,20,23,35,36,36–38], the method's significant computational demand hinders its applicability for large-scale numerical exploration.

Recently, benefiting from advancements in discrete differential geometry (DDG) theory, a new numerical framework has emerged. Initially employed in computer graphics, the DDG-based method has recently been applied to the structural analysis of mechanical systems, particularly for slender elastic structures such as rods and shells [39–41]. This approach is valued for its computational efficiency and numerical robustness [42]. Due to its physical accuracy, numerical robustness and computational efficiency in handling geometrically nonlinear deformations, the DDG-based method is naturally suited for the simulation of thin elastic structures. Moreover, the node-based formulation in DDG can easily deal with complex interactions with the external environment, e.g. frictional contact, fluid–structure interactions and multi-physical actuations, which would be hard for traditional finite element-based methods. Recently, a novel, DDG-based one-dimensional discrete axisymmetric model has been developed and has shown extraordinary performance in simulating the thin elastic shell undergoing large deformation, contact indention and magnetic actuation [43]. Here, we employ this newly developed numerical framework to systematically investigate the stability and snap-through eversion of an axisymmetric shell under contact indention.

In this study, we first focus on the mechanical response and stabilities of an axisymmetric shell under point indentation. We further explore the snap-through inversion of spherical shells

when indented by a rigid spherical indenter. We then examine two extreme cases of point loading (where the rigid spherical indenter is assumed to have a radius of zero) and plate loading (where the indenter is considered to have an infinite radius), and aim to bridge the gap between them to provide a comprehensive understanding of the contact-induced snap-through in an axisymmetric shell. We also carried out FEM simulations to validate the analysis derived from the discrete model.

This paper is organized as follows. In §2, we describe the problem set-up. In §3, we introduce the discrete numerical model, including the incremental potential contact method. In §4, the phenomenon of contact-induced shell snapping is systematically investigated. The paper concludes with remarks and potential directions for future research in §5. The one-dimensional symmetric FEM simulations and three-dimensional full-scale FEM simulations for validation are presented in appendix A and appendix B, respectively.

2. Problem set-up

Referring to figure 1*a*, we consider a spherical shell subjected to indentation by a rigid spherical indenter. The shell has a radius R, the meridional range angle is $\phi \in [\hat{\phi}, \pi/2)$ and the spherical indenter has a radius of r. The external compressive force was denoted as F. To allow the shell eversion, we use a sliding boundary condition at the bottom, i.e. the first node at the shell bottom is fixed along the $\hat{Z}$ direction but is free to move along the $\hat{R}$ direction. Due to the boundary nonlinear contact (the boundary condition will change due to contact and thus needs to be updated during loading) between the rigid indenter and flexible shell, the system would experience a nonlinear deformation when the indenter was compressed (figure 1*b*) and when the compressive distance is beyond a threshold, the system would undergo a sudden change, which is known as shell eversion (i.e. snap-through buckling), see figure 1*c*. In the following sections, we employ a discrete numerical framework to investigate the nonlinear deformation of the axisymmetric shell and the associated contact-induced snap-through behaviours.

3. Numerical model

In this section, we discuss the numerical framework for the nonlinear mechanics analysis of an axisymmetric shell under contact indentation. The geometrically nonlinear deformation of an axisymmetric shell is formulated based on DDG theory [43], and the contact between the non-penetration contact is achieved by the incremental potential method [44]. The nonlinear system is numerically solved by the Newton–Raphson method, as described in Huang *et al*. [45].

(a) One-dimensional discrete shell model

The one-dimensional discrete shell model introduced in Huang *et al*. [43] will be utilized for analysing shell deformation and eversion as follows.

Degrees of freedom. Referring to figure 2*a,b*, due to the axisymmetric constraint, the three-dimensional problem considered in the current study can be simplified into a one-dimensional system in the $\hat{R}-\hat{Z}$ plane. First, a curvilinear coordinate, $s = \mathbf{x}(r, z) \in \mathcal{R}^2$, is used to describe the configuration of a rotational symmetric three-dimensional shell system. Next, the one-dimensional curved contour is discretized into N nodes, such that rise to a vector $2N$-sized degrees of freedom vector,

$$\mathbf{q}_s = [\mathbf{x}_0, \mathbf{x}_1, \ldots, \mathbf{x}_i, \ldots, \mathbf{x}_{N-1}], \tag{3.1}$$

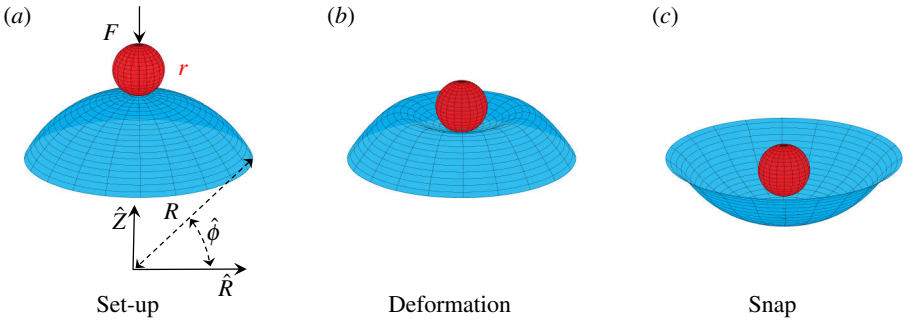

Figure 1. Schematic for the snap-through buckling of a spherical shell under indentation by a rigid spherical indenter. (*a*) Set-up of the system. (*b*) Indentation-induced deformation of the shell. (*c*) Eversion of the shell after snap.

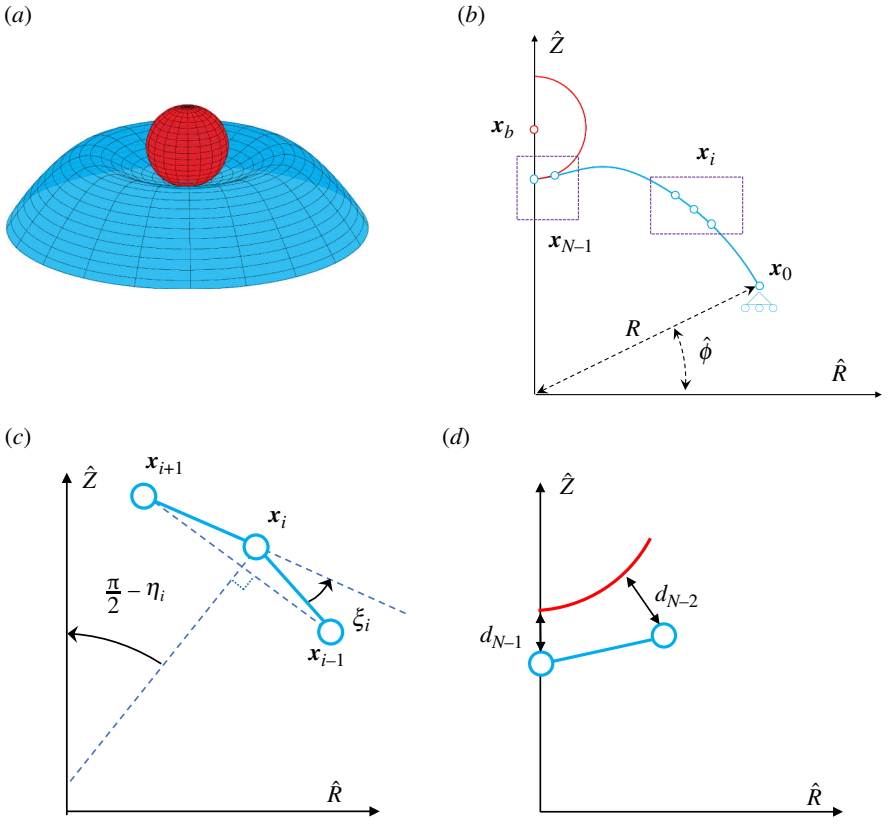

Figure 2. Basic set up of the one-dimensional discrete shell model for an axisymmetric shell: (*a*) Three-dimensional view of the deformation of axisymmetric shell (blue) under loading along its symmetry axis through a rigid spherical indenter (red). (*b*) Two-dimensional projection of the deformed shell, in which the blue line represents the deformed shell, the red half-circle represents the outer surface of the rigid indenter. The $\hat{Z}$-axis is the symmetry axis of the shell whereas $\hat{R}$-axis is in the radial direction. The shell contour is discretized into $N-1$ elements with N nodes from x_0 to x_{N-1}. (*c*) Typical $(i-1)$-th and i-th elements depicting their location $\pi/2 - \eta_i$ and the relative rotation ξ_i. (*d*) The method to calculate the distance between the boundary of spherical indenter and the shell element.

where $\mathbf{x}_i \equiv [r_i, z_i]$. The edge vector between two consecutive nodes is,

$$\mathbf{e}^i = \mathbf{x}_{i+1} - \mathbf{x}_i, \tag{3.2}$$

and its tangent vector and normal vector can be formulated as:

$$\mathbf{t}^i = \frac{\mathbf{e}^i}{l^i} \quad \text{and} \quad \mathbf{n}^i \cdot \mathbf{t}^i = 0, \tag{3.3}$$

where $l^i = \|\mathbf{e}^i\|$ is its length. To follow the convention, we use subscripts to denote quantities associated with the nodes and superscripts when associated with edges. Also, the average is used to transfer the node-based quantity to the edge-based quantity, e.g. the radius of i-th edge is denoted as:

$$r^i = \frac{1}{2}(r_i + r_{i+1}), \tag{3.4}$$

and the Voronoi length associated with the i-th node is given by:

$$l_i = \frac{1}{2}(l^{i-1} + l^i). \tag{3.5}$$

Discrete strains. We next formulate the discrete macro strains (stretching strains and bending curvatures) for the one-dimensional discrete shell system. The stretching strain of i-th edge along the meridional direction is straightforward,

$$\epsilon^i_{11} = \frac{l^i}{\bar{l}^i} - 1, \tag{3.6}$$

and the stretching strain of i-th edge along the circumferential is related to the expansion of the circle,

$$\epsilon^i_{22} = \frac{r^i}{\bar{r}^i} - 1. \tag{3.7}$$

The coupling between the meridional direction and the circumferential direction for shearing is zero, i.e.

$$\epsilon^i_{12} = \epsilon^i_{21} = 0. \tag{3.8}$$

The bending curvature at a material point i has two components: (i) the curvature along the meridional direction and (ii) the curvature perpendicular to the meridional direction. The curvature along the meridional direction is identical to the curvature formulation of a planar beam, i.e. is related to the relative positions of the three consecutive nodes,

$$\kappa_{11,i} = \frac{2\tan(\xi_i/2)}{l_i}, \tag{3.9}$$

where ξ_i is the turning angle between the three consecutive nodes (figure 2*c*); the one perpendicular to the meridional direction is determined by the change of direction of the surface normal, as:

$$\kappa_{22,i} = \frac{\cos(\eta_i)}{r_i}, \tag{3.10}$$

where η_i is the orientation angle, which is evaluated by the surface normal vector, $\mathbf{n}_i$, and the R axis, as displayed in figure 2*c*. Similarly, the coupling between the meridional direction and the circumferential direction for bending is zero, i.e.

$$\kappa_{12,i} = \kappa_{21,i} = 0. \tag{3.11}$$

Discrete energies. Based on the Kirchhoff–Love hypothesis, the total elastic energy of an axisymmetric shell in discrete form is the sum of stretching and bending energies, as:

$$W^e = \sum_{i=0}^{N-2} \pi \bar{r}^i \left(\mathcal{S}^i \cdot \mathbb{D}_s \cdot \mathcal{S}^i\right) \bar{l}^i + \sum_{i=1}^{N-2} \pi \bar{r}_i \left(\mathcal{B}_i \cdot \mathbb{D}_b \cdot \mathcal{B}_i\right) \bar{l}_i, \tag{3.12}$$

where the discrete local strain tensors are:

$$\mathcal{S}^i = \begin{bmatrix} \epsilon^i_{11} & \epsilon^i_{12} \\ \epsilon^i_{21} & \epsilon^i_{22} \end{bmatrix} \quad \text{and} \quad \mathcal{B}_i = \begin{bmatrix} \kappa_{11,i} - \bar{\kappa}_{11,i} & \kappa_{12,i} - \bar{\kappa}_{12,i} \\ \kappa_{21,i} - \bar{\kappa}_{21,i} & \kappa_{22,i} - \bar{\kappa}_{22,i} \end{bmatrix}, \tag{3.13}$$

where $\bar{\kappa}$ is the curvature of the shell in the undeformed configuration, and the stiffness tensors are (with Young's modulus E, Poisson's ratio ν and shell thickness h):

$$\mathbb{D}_s = \frac{Eh}{1-\nu^2}\begin{bmatrix} 1 & \nu \\ \nu & 1 \end{bmatrix} \quad \text{and} \quad \mathbb{D}_b = \frac{Eh^3}{12(1-\nu^2)}\begin{bmatrix} 1 & \nu \\ \nu & 1 \end{bmatrix}. \tag{3.14}$$

Here, a linear elastic constitutive law is used to reduce the model from three dimensions to one dimension, and the three-dimensional shell with no homogeneous constitutive law can be found in Liu *et al.* [46]. Also, as the thin shell with a small thickness-to-radius ratio is considered, the physical strains are of the order of h/R and are generally small, such that the linear elastic constitutive model can be a good approximation.

(b) Incremental potential contact method

Here, we review the incremental potential formulation [44] for contact between a spherical indenter and the axisymmetric shell. The spherical indenter of size r is located at $\mathbf{x}_b$. The minimum distance between the i-th node and the spherical indenter is denoted as:

$$d_i = \|\mathbf{x}_i - \mathbf{x}_b\| - r, \tag{3.15}$$

referring to figure 2*d*. To achieve a non-penetration condition between the rigid indenter and a flexible shell, i.e. $d_i > 0$, we employ an incremental potential between the approaching elements [47]. A smooth log-barrier potential U_i^c with C^2 continuity is employed when the i-th node is within a critical distance with the rigid surface [47]:

$$W_i^c = \begin{cases} -K_c \left(d_i - \hat{d}\right)^2 \log(d_i/\hat{d}) & \text{when } 0 \le d_i < \hat{d}, \\ 0 & \text{when } d_i \ge \hat{d}, \end{cases} \tag{3.16}$$

where d_i is the minimum distance between i-th node and the target object, $\hat{d}$ is the barrier parameter and K_c is the contact stiffness. The log-barrier energy is zero when the distance is larger than $\hat{d}$, and the repulsive interaction gradually increases as the distance decreases within $\hat{d}$. The repulsive cost goes to infinite if d_i approaches zero. The total contact potential is the sum of all contact elements,

$$W^c = \sum_{i \in \mathcal{C}} W_i^c \quad \text{with} \quad 0 \le d_i < \hat{d}, \tag{3.17}$$

where $\mathcal{C}$ are the set of contact primitives.

(c) Numerical solver

Finally, we formulate the discrete equations of motion of an indenter-shell system. The total degrees of freedom vector is the sum of nodes on the shell and the position of an indenter,

$$\mathbf{q} = [\mathbf{q}_s, \mathbf{x}_b], \tag{3.18}$$

and we use the principle of virtual work to determine the governing equations for the nonlinear system,

$$\delta W^e + \delta W^c - \delta W^{\text{ext}} = 0, \tag{3.19}$$

where W^{ext} is the work from the external actuation. With the principle of virtual work, we can find the global residual vector,

$$\mathbf{R} = \frac{\partial W^e}{\partial \mathbf{q}} + \frac{\partial W^c}{\partial \mathbf{q}} - \frac{\partial W^{\text{ext}}}{\partial \mathbf{q}}, \tag{3.20}$$

and the system is in equilibrium when the residual vector is zero,

$$\mathbf{R} = \mathbf{0}. \tag{3.21}$$

We use gradient descent to iteratively optimize the discrete system until the relative error is with the tolerance [45]. Also, to deal with the discontinuous fold point that is associated with snap-through, the inertial and damping terms are included in the discrete system, known as the dynamic relaxation method. It is worth noting that we use MATHEMATICA symbolic manipulation to derive the closed-form formulations of the gradient vectors and the Hessian matrices of the discrete potentials, such that our numerical solver is fully implicit.

4. Results

In this section, we present the findings from our numerical exploration. We first discuss the mechanics of a spherical shell under point indentation, and next extend to the contact-induced indention by a rigid spherical indenter with finite radius. A simple geometric model for the contact-induced indention is later formulated. Finally, we bridge the gap between the point-loaded snapping and the plate-loaded snapping of a bistable axisymmetric shell.

(a) Shell mechanics under point indentation

We first examine the nonlinear mechanical response of a spherical shell under a concentrated load at the pole (inset of figure 3*a*), during which the spherical indenter is assumed to be a single point. The mechanics of a spherical shell is determined by its material properties as well as geometric parameters, including meridional angle, $\hat{\phi}$ and normalized shell thickness, h/R [3,7]. We use shell radius $R = 1.0$ m, Young's modulus $E = 1$ MPa and Poisson's ratio $\nu = 0.5$, and the resulting bending rigidity $D = Eh^3/12(1-\nu^2)$. The shell contour is discretized along its meridional direction into $N = 200$ nodes and the relative tolerance error for the stop is $1e-6$. To achieve the shell eversion, we use an axisymmetric condition at the top and a sliding boundary condition at the bottom.

Figure 3*a* shows the normalized force, $Fh/2\pi D$, as a function of relative midpoint displacement, w/R, at various meridional angles $\hat{\phi}$ and $h/R = 0.02$. For deep shells with $\hat{\phi} < 1.1$, bistable behaviour is observed with a minimum load below zero. At $\hat{\phi} > 1.1$, the shell behaviour transitions from bistable to monostable, with a local load minimum above zero. At a very large meridional angle, e.g. $\hat{\phi} = 1.3$, the normalized force increases monotonically without snap-through behaviour. Figure 3*b* shows the force–displacement relations with different normalized shell thickness, h/R, ranging from 0.01 to 0.08 at a given meridional angle, $\hat{\phi} = 1.0$. Similarly, the force–displacement curves exhibit bistable, monostable and monotonic behaviours of the shell with increasing h/R.

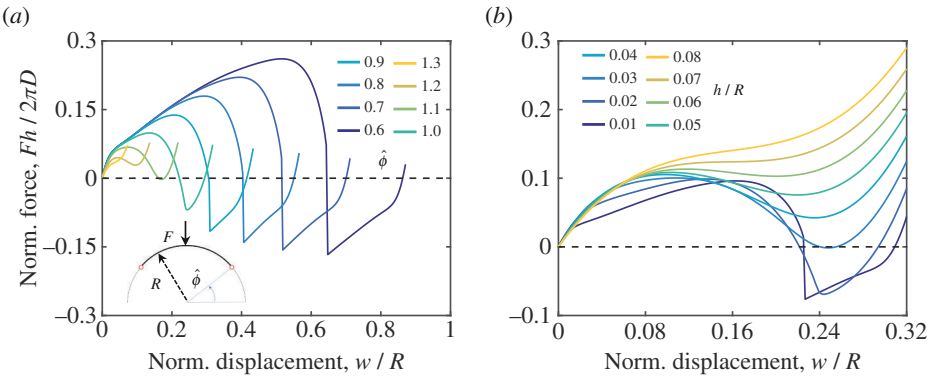

Figure 3. Dependence of the normalized reaction force on the indenter, $Fh/2\pi D$, as a function of the normalized relative midpoint displacement, w/R, for a spherical shell with different geometric parameters: (*a*) with fixed shell thickness of $h/R = 0.02$ and different meridional angles in the range of $\hat{\phi} \in [0.6, 1.3]$; (*b*) with fixed meridional angle of $\hat{\phi} = 1.0$ and different shell thickness in the range of $h/R \in [0.01, 0.08]$.

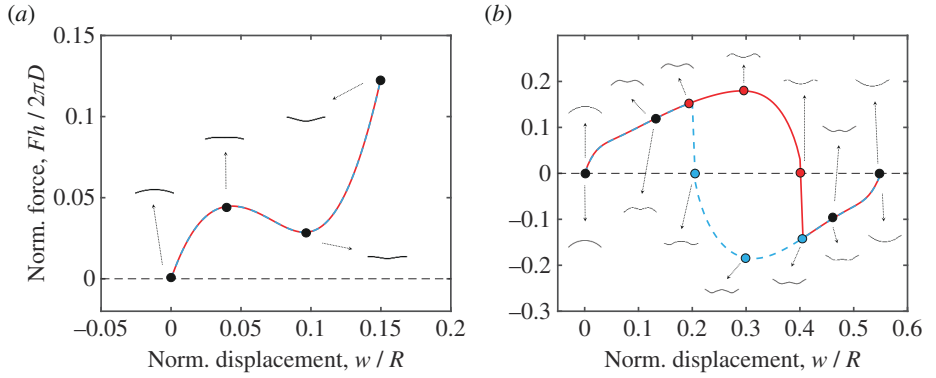

Figure 4. The force–displacement curves in the loading and unloading paths and the associated configurations of a bistable shell with meridional angle (*a*) $\hat{\phi} = 1.2$ and (*b*) $\hat{\phi} = 0.8$. The shell thickness is fixed as $h/R = 0.02$.

To highlight the differences between a deeper shell and a shallower shell, we present the loading and unloading processes of the spherical shell. Figure 4*a,b* show the relationship between the normalized force and the normalized pole displacement of monostable and bistable shells, respectively, for both the loading (solid red curve) and the unloading (dashed blue line) cases, in which the shell thickness is fixed as $h/R = 0.02$, and the meridional angles are $\hat{\phi} = 0.8$ and 1.2, respectively. The associated configuration evaluations are also given as the zoom-in figures in figure 4. We can see the force–displacement responses during the loading and unloading processes are different for the two shells. For the shallow shell, i.e. the shell with $\hat{\phi} = 1.2$, the loading and unloading curves are fully overlapped, while the significant hysteresis behaviour can be found for the deep shell ($\hat{\phi} = 0.8$).

The effects of geometric parameters on shell mechanics can be systematically presented by a phase diagram shown in figure 5. By sweeping the parameter space, a phase diagram can be constructed as in figure 5*b*, in which the $\hat{\phi}$ - h/R space is divided into three regions, i.e. bistable (red), monostable (blue) and monotonic (green) regions. Note that here we employ a displacement boundary condition, i.e. the pole is manually moved from top to bottom, such that the negative force may be achievable during loading. The three states are classified based on the force–displacement curve, i.e. (i) monotonous is when the force always increases with

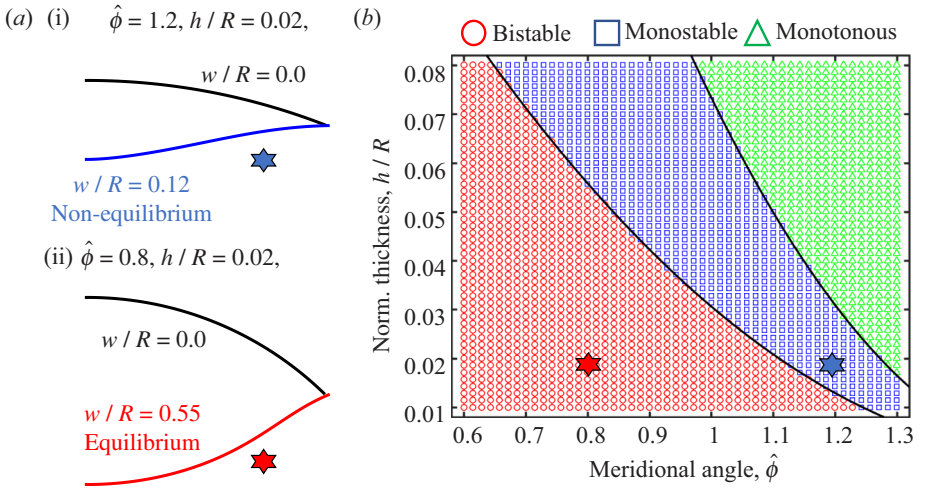

Figure 5. Three characteristic snap-through behaviours of a spherical shell. (*a*) Configurations of a (*i*) monostable and (ii) bistable shell. (*b*) Phase diagram of the stability in the space of h/R - $\tilde{\phi}$: monotonous (green), monostable (blue) and bistable (red). Note that the deformed configuration in (i) is randomly selected and is not equilibrium, while the shape in (ii) is within the equilibrium.

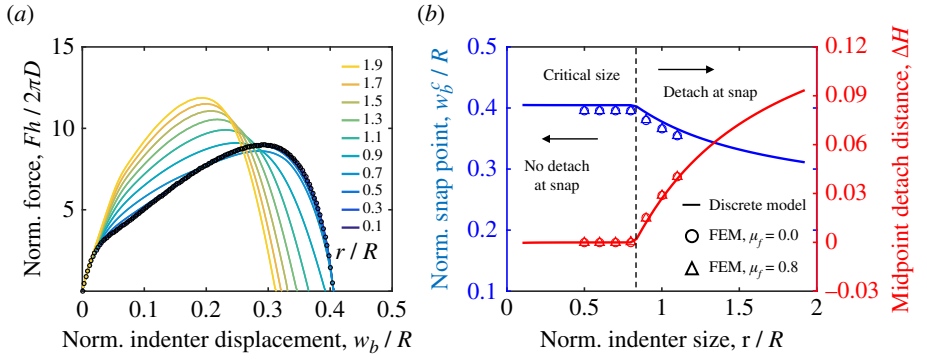

Figure 6. Behaviour of a spherical shell under indentation by a rigid spherical indenter; the meridional angle is $\hat{\phi} = 0.8$, and the shell thickness is $h/R = 0.02$. (*a*) Normalized probe force, $FR/2\pi D$, versus normalized indentation displacement, w/R, for different indenter size, r/R. The open circles are results from the point indention. (*b*) Critical snap displacement of the indented ball, w_b^c/R, and the detach distance between the shell pole and indenter, ΔH, as a function of the normalized indenter size, r/R, from discrete model (solid lines), FEM with friction coefficient $\mu_f = 0.0$ (open circles) and FEM with friction coefficient $\mu_f = 0.8$ (open triangles).

increasing displacement, (ii) monostable is when the force may decrease as the displacement increases, but the force is always positive, and (iii) bistable is that the force can be negative during the displacement loading.

The two cases depicted in figure 5*a* (which are also the cases presented in figure 4) are labelled in the phase diagram. It is interesting to see that the boundaries separating different zones in the phase diagram can be accurately captured by the relationship derived based on the ratio between the bending and stretching energy of the shell [3,7], given by:

$$\frac{h}{R} = \frac{1}{\lambda_d}\sqrt{12(1-\nu^2)}\,(\frac{\pi}{2} - \hat{\phi})^2, \tag{4.1}$$

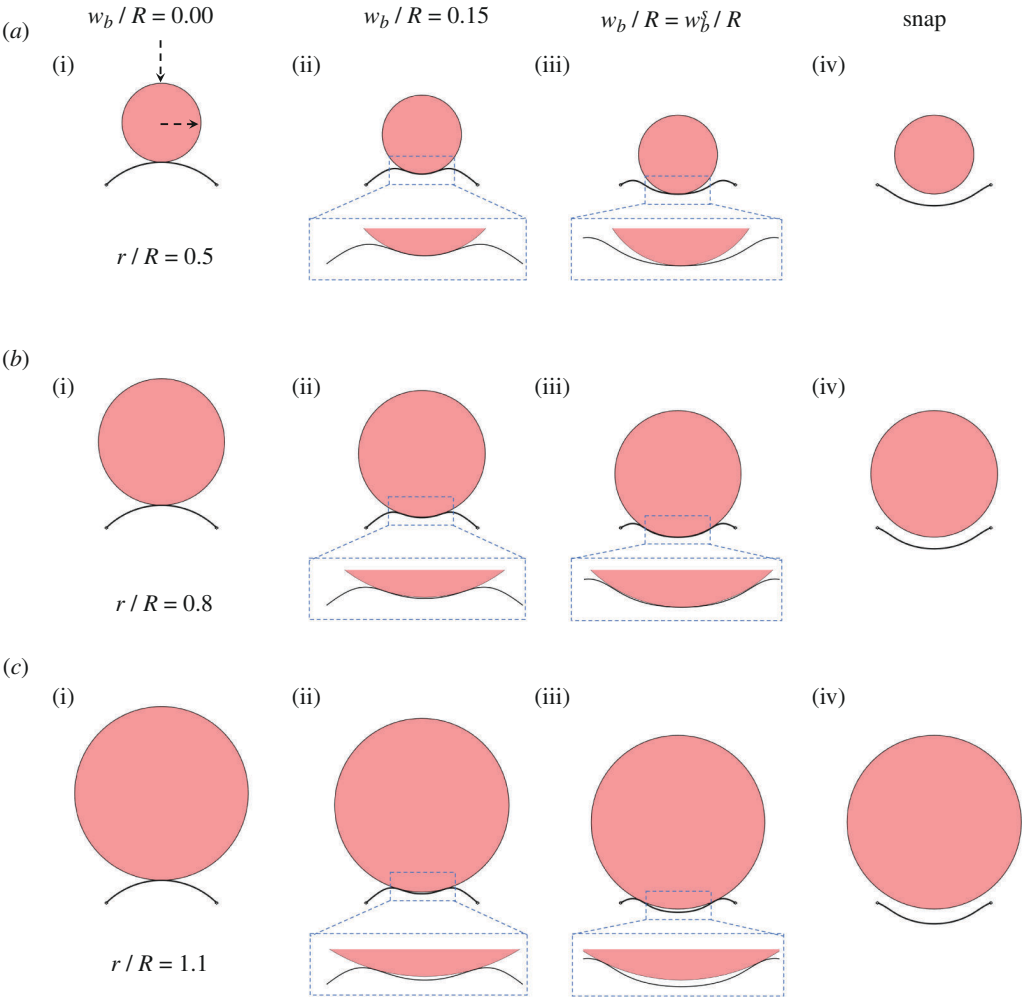

Figure 7. Configurations of a spherical shell under indentation by a rigid spherical indenter. (*a*) $r/R = 0.5$. (*b*) $r/R = 0.8$. (*c*) $r/R = 1.1$. The indentation depth is increasing from (i) to (iv). Note that the configurations in column (iii) are the critical snapping state.

where λ_d is a dimensionless fitting parameter, and $\lambda_d = 5.65$ gives rise to the boundary between the bistable phase and monostable phase that is consistent with the result from Taffetani *et al*. [3]. In Taffetani *et al*. [3], the diagram for a shell cap was divided into two phases: (i) monostable and (ii) bistable, and the boundary is due to the ratio between the bending energy and stretching energy, and is by equation (4.1) with $\lambda_d = 5.65$. Our result is consistent with this finding, i.e. the boundary between monostable and bistable regions in the current study follows the same equation with $\lambda_d = 5.7$. Moreover, we here find one more phase, monotonous, and the boundary between the monostable and monotonous regions is also accurately described by equation (4.1) with $\lambda_d = 3.65$.

(b) Shell snapping under contact indentation

We now turn our attention to the snap-through behaviour of axisymmetric spherical shells under indentation by a rigid spherical indenter (inset in figure 6*a*), where the boundary nonlinear contact is involved. With our model, it is straightforward to incorporate the indenter

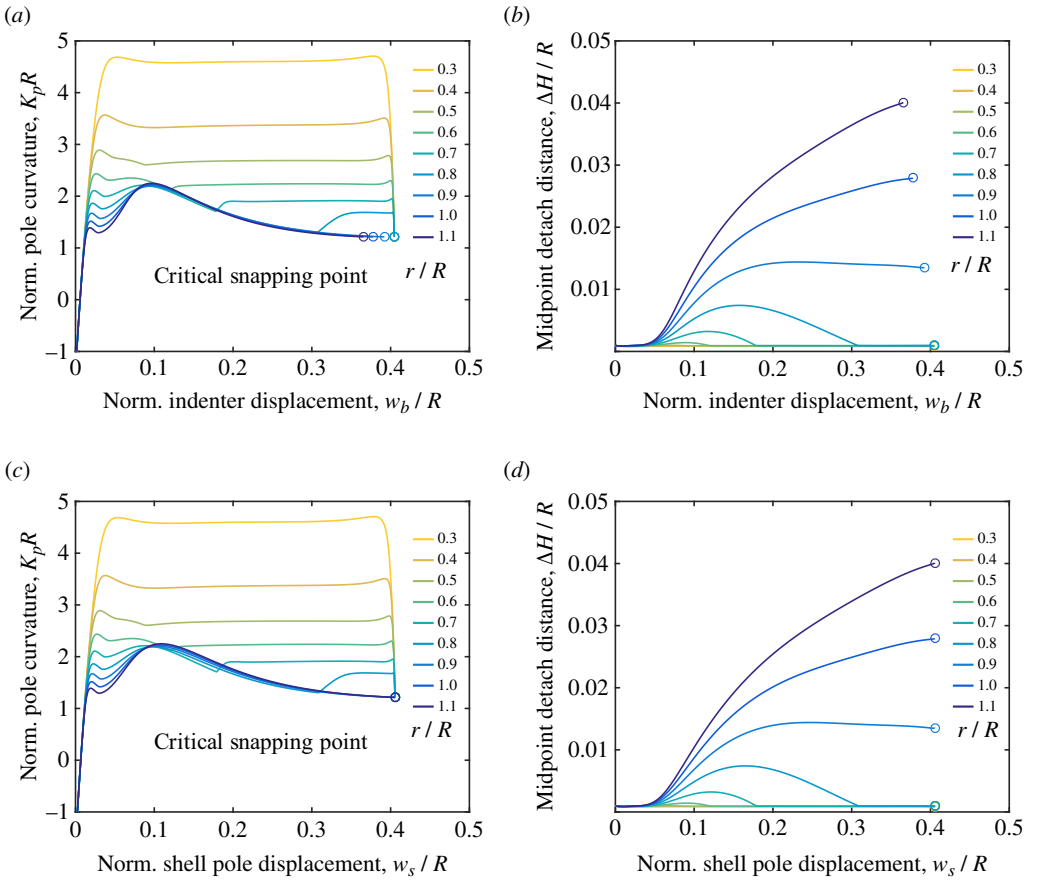

Figure 8. Shell pole curvature, κ_p, normalized by shell radius, R, as a function of (*a*) relative indentation displacement, w_b/R, and (*c*) shell pole displacement, w_s/R. Normalized detached distance between the shell pole and the indenter surface, $\Delta H/R$, as a function of (*b*) relative indentation displacement, w_b/R, and (*d*) shell pole displacement, w_s/R. The relative indenter size is changed from $r/R = 0.3$ to $r/R = 1.1$.

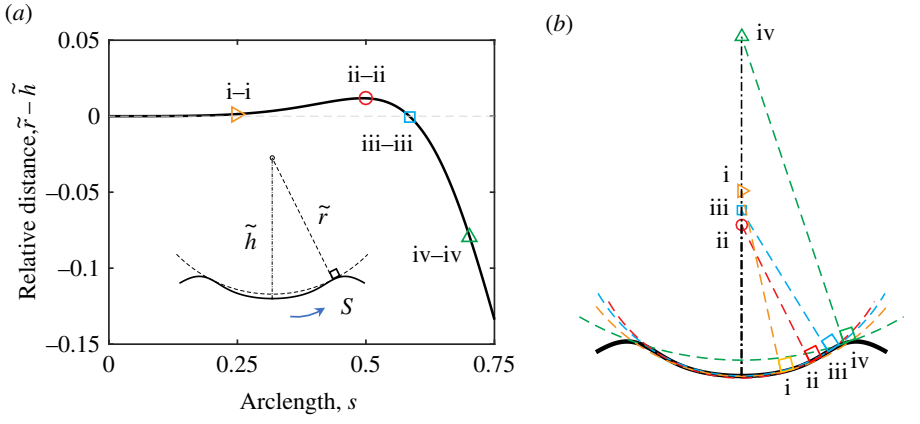

Figure 9. Features of the universal shell configuration at the point of snapping. (*a*) The relative distance between the circle radius and the centre height, $\tilde{r} - \tilde{h}$, as a function of the shell arc-length parameter. Here, we fix the geometric parameters of the shell as $\bar{\phi} = 0.8$ and $h/R = 0.02$. The contact circle radius is $\tilde{r}$ and its centre height is $\tilde{h}$. (*b*) Some representative configurations in our geometric analysis.

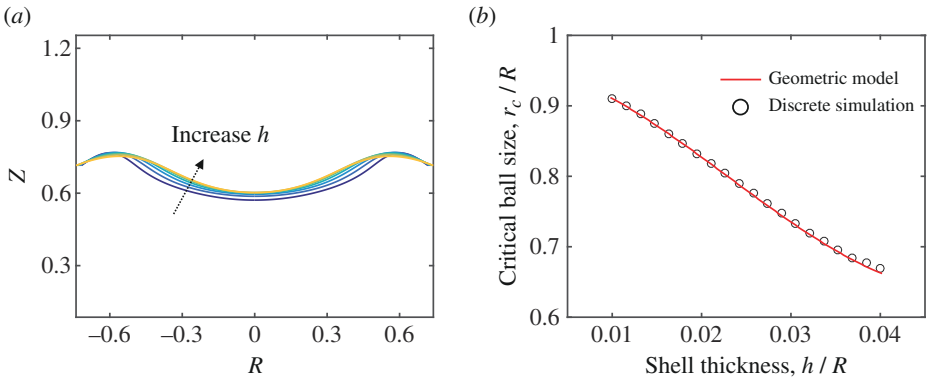

Figure 10. Characteristics of spherical shells with varying thickness near the snapping point. (*a*) The configurations of spherical shell near the snapping point with a fixed meridional angle, $\hat{\phi} = 0.8$, and varying thickness, $h/R \in [0.1, 0.4]$. (*b*) Critical indenter size, r_c/R, as a function of shell thickness, h/R, from both numerical simulations and geometric model.

shape with a contact model to study the contact-induced snapping of a spherical shell. The radius of the rigid spherical indenter is taken to be r, the spherical shell has a radius R, thickness h, meridional angle $\hat{\phi}$, Young's modulus E and Poisson's ratio ν. The contact interface is assumed to be friction-free, and the contact parameters are $K_c = 1e8$ Pa and $\hat{d} = 1e-3$ m after a convergence study. Again, the shell contour is discretized into $N = 200$ nodes, and an axisymmetric condition at the top and a sliding boundary condition at the bottom are employed.

For this contact problem, the mechanical response of the shell is nonlinear. The indentation force F can be calculated for the given displacement of the indenter, w_b. As w_b increases, the shape of the shell evolves until w_b reaches a critical value, at which the spherical shell would suddenly evert and snap to another equilibrium configuration.

Figure 6*a* shows the normalized reaction force, $FR/2\pi D$, as a function of the normalized indentation displacement, w_b/R. In these simulations, the meridional angle $\hat{\phi} = 0.8$, the shell thickness $h/R = 0.02$ and a range of indenter sizes $r/R \in [0.1, 2.0]$ are considered. For all values of r/R, when the force reaches zero, which occurs at a critical displacement w_b^c, the shell suddenly snaps and transitions to another equilibrium configuration. This transition occurs at a critical displacement, denoted as w_b^c. When the indenter size is small compared with the shell radius (e.g. $r/R < 0.8$), the critical displacement is constant and independent of the indenter size. However, when the indenter size exceeds a critical value (e.g. $r/R > 0.9$), the critical displacement decreases with increasing r/R. Figure 6*b* shows, on the left side (blue), the critical indentation displacement w_b^c as a function of the corresponding indenter size r/R, clearly exhibiting a transition highlighted by the vertical dashed line.

To gain deeper physical insights, we illustrate the shape evolution of the deformed shells under the compression by spherical indenter in figure 7, in which three characteristic cases with different indenter sizes (i.e. $r/R = 0.5, 0.8$ and 1.1) are highlighted. We observe that the indenter size plays an important role in the shell behaviour. When the indenter radius is small (case with $r/R = 0.5$, figure 7*a*), the shell pole always remains in contact with the indenter until snapping. However, for larger indenters (case with $r/R = 1.1$, figure 7*c*), the shell pole detaches from the indenter upon reaching a certain indentation displacement before snapping. This detachment is accompanied by the change of the contact point from the pole towards the outer edge. The case with $r/R = 0.8$ (figure 7*b*) shows a peculiar situation where the shell pole slightly detaches, then comes back into contact before snapping. Intuitively, we recognize that the limiting case must be true, i.e. for an indenter of infinite radius of curvature (flat punch), it is much more likely that detachment between the shell pole and the indenter would occur before snapping.

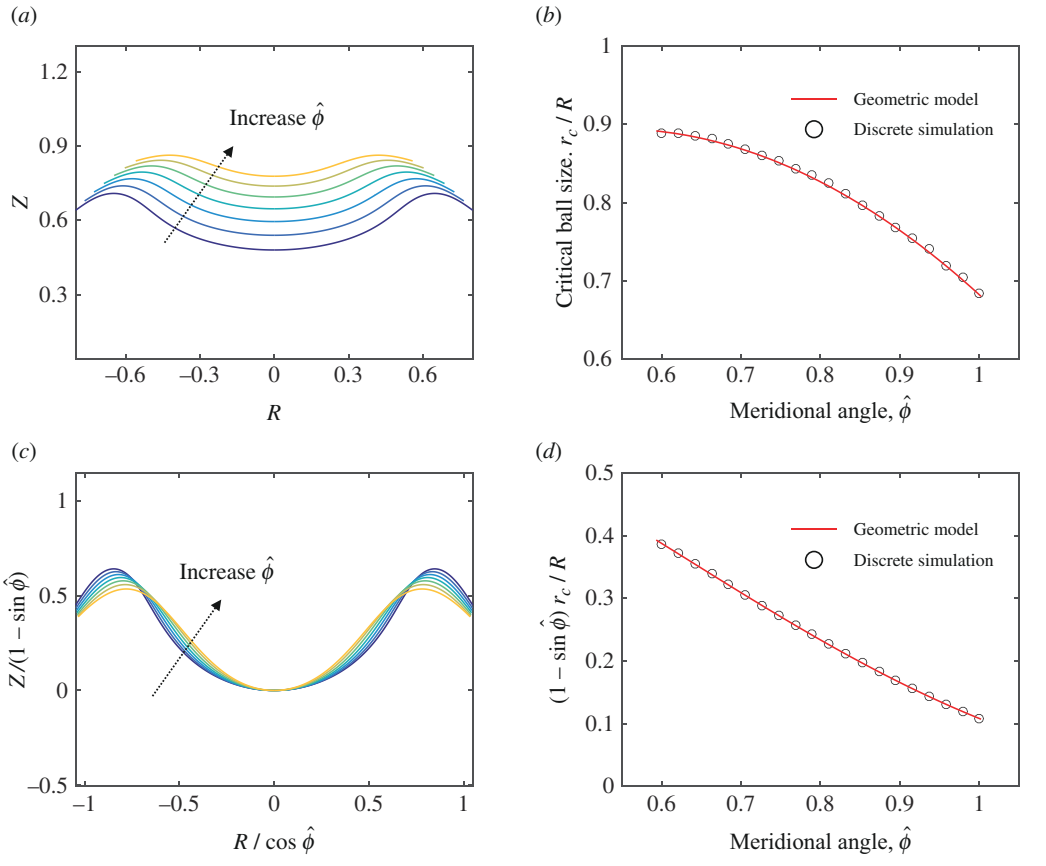

Figure 11. Characteristics of spherical shells with varying meridional angle near the snapping point. (*a*) Configurations for fixed thickness, $h/R = 0.02$, and varying meridional angle, $\hat{\phi} \in [0.6, 1.0]$. (*b*) Critical indenter size, r_c/R, as a function of meridional angle, $\hat{\phi}$, from both contact-based simulation and geometric model. (*c*) The normalized configurations of the critical snapping shell (the R direction is normalized by $\cos\hat{\phi}$ and the Z direction is normalized by $1-\sin\hat{\phi}$. (*d*) The normalized critical indenter size (by $1-\sin\hat{\phi}$) as a function of $\hat{\phi}$.

Our quantitative study here provides a detailed characterization of this phenomenon. We plot the separation distance between the shell pole and the indenter tip (ΔH) in figure 6*b* (see the red curve) as a function of the normalized indenter size (r/R). It is clear that the critical indenter size causing the transition in behaviour for both w_b^c/R and ΔH coincide, providing evidence that such transition is attributed to the detachment between the indenter and the spherical shell at the snapping point. Three-dimensional FEM analysis using ABAQUS for both frictional and frictionless contact is also carried out for cross-validation. Details of the FEM model can be found in appendix A.

For bistable shells, figure 8*a* shows the normalized curvature at the pole, $\kappa_p R$, as a function of the normalized indentation displacement, w_b/R for different indenter size. It shows that the pole curvature varies significantly during indentation, but reaches the same value at snapping. Figure 8*b* shows the detach distance between the shell pole and the indenter, $\Delta H/R$, as a function of displacement, w_b/R for different indenter sizes. It confirms that, depending on the size of the indenter, there are three contacting modes before snapping: (i) continuous contact

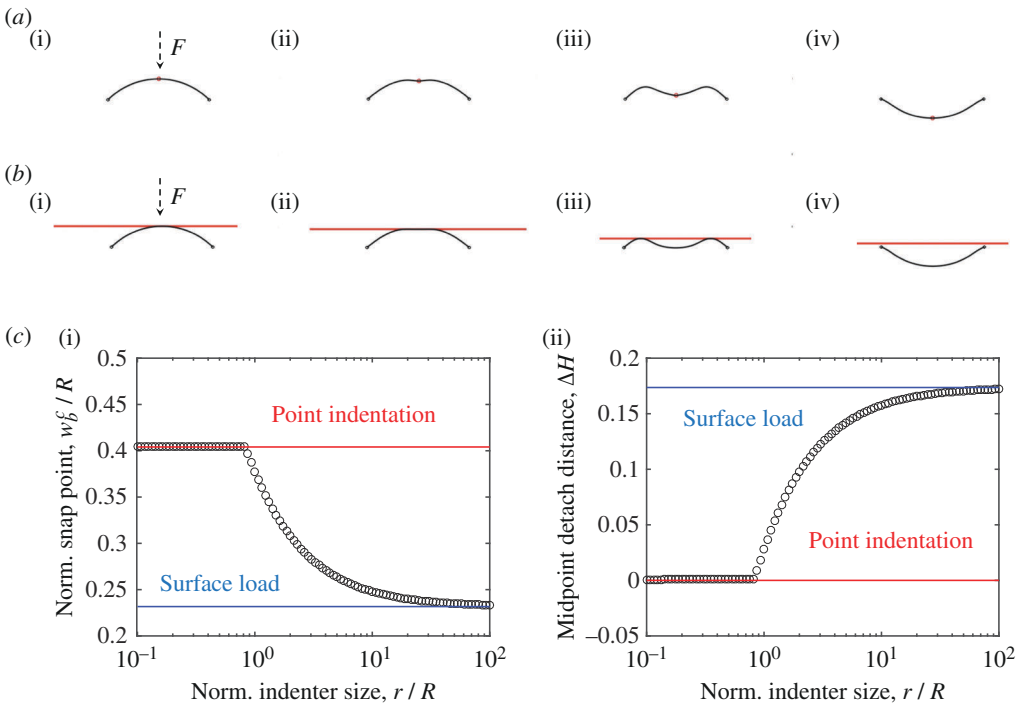

Figure 12. Configuration evaluations of a spherical shell under (*a*) point actuation ($r \to 0$) and (*b*) plate compression ($r \to \infty$). (*c*) (i) Midpoint displacement at critical snapping, w_s/R, and (ii) the minimum distance between shell midpoint and indenter at the critical snapping, $\Delta H/R$, as a function of relative indenter size, r/R.

($r/R \le 0.5$), (ii) contact followed by detachment and then recontact ($0.6 \le r/R \le 0.8$), and (iii) contact followed by detachment ($r/R \ge 0.9$).

Interestingly, for a shell with prescribed meridional angle, $\hat{\phi}$, and relative thickness, h/R, its critical pole position and deformed shape at snapping are identical for different sizes of the indenter. This similarity arises because, at the snapping point, the externally applied force is zero, making the configuration independent of contact position and contact force. Instead, it is intrinsically determined by the shell itself.

(c) Geometric analysis for the contact-induced snapping

We also examine the underlying reason for the critical indenter size that marks the transition in snapping displacement in figure 6*b*. Since the shape of the shells at the snapping point is universal and independent of the indenter size, we can expect the critical condition for snapping to be purely geometric. Therefore, a simple geometrical model can be constructed for the analysis of contact-induced snapping. Figures 6*b* and 7 show that the difference between the constant critical indentation regime and the decaying regime is the contact point at snapping, i.e. changing from full contact (e.g. figure 7*a*(iii),*b*(iii)) to partially detach (figure 7*c*(iii)). This geometric feature is depicted by the inset in figure 9*a*; because the configuration of the deformed shell at the critical snapping point is known and universal, we can compute its rotation orientation and the associated perpendicular line for any given point; then, its intersection with the vertical axis is defined as the circle centre, and the corresponding radius $\tilde{r}$ and height $\tilde{h}$ can be easily determined based on geometric analysis. In figure 9*a*, we plot the relative distance between the circle radius and its centre height, $\tilde{r} - \tilde{h}$, as a function of the shell arc-length parameter, s, which is starting from the shell pole. The illustration of the

corresponding geometric relation for four different states (marked by symbols in figure 9*a*) is also given in figure 9*b*. If $\tilde{r} - \tilde{h} > 0$ (i.e. case ii–ii), the indenter would penetrate the shell, which is physically impossible, such that the indenter can only make contact with the pole of the shell by moving upwards slightly, and the loading curvature is identical to the point indention; on the other side, once $\tilde{r} - \tilde{h} < 0$ (i.e. case iv–iv), the indenter can contact the intermediate region of the shell but stays separate from the pole point, and, as a result, a detached distance can be found and the critical snapping point shows a variation compared with the ideal point indention, in which the force can only be applied at its midpoint. Therefore, $\tilde{r} - \tilde{h} = 0$ (corresponding to the case of iii–iii) could be used as the criterion for judging the form of contact at the critical snapping state, and consequently, the critical indenter size regarding the transition of the critical indentation displacement can be determined.

Figure 10*a* presents the shape of shells with a fixed meridional angle $\hat{\phi} = 0.8$ at snapping for various thicknesses, $h/R \in [0.1, 0.4]$. The dependence of the critical indenter size, r_c/R, on the shell thickness, h/R, is shown in figure 10*b*, where both discrete simulations and geometric analysis results are provided, showing quantitative agreement. Notably, the critical indenter size exhibits an almost linear relationship with the shell thickness when the shell is thin (i.e. $h/R \lesssim 0.035$). This indicates that the thickness effect on the snapping behaviour of spherical shells is linear, at least for small thicknesses.

On the other hand, the effect of the meridional angle of the shell, $\hat{\phi}$, on the critical indenter size—see figure 11*a*, which shows the critical snapping configurations of the shells with a fixed thickness, $h/R = 0.02$—varies noticeably with the meridional angle, $\hat{\phi} \in [0.6, 1.0]$. Similarly, figure 11*b* shows the dependence of critical indenter size, r_c/R, on the shell meridional angle, $\hat{\phi}$, in which good agreement between the geometric analysis and our discrete simulation is evident. Interestingly, even though the relationship between r_c/R and $\hat{\phi}$ is nonlinear, we can easily shift it to a linear relation if the critical indenter size is normalized by $(1 - \sin\hat{\phi})$ (see figure 11*d*), simply because the configurations of the shells with different meridional angles show the self-similarity, which can be confirmed by normalizing the configuration at the R direction by $\cos\hat{\phi}$ and the Z direction by $1 - \sin\hat{\phi}$, respectively, as shown in figure 11*c*.

(d) From point indention to plate indention

All examples we have investigated so far involved finite indenter size. We now extend the range of the indenter radius, r, to two extreme cases: the point indentation mode ($r \to 0$) and the flat plate indentation mode ($r \to \infty$). The characteristic behaviours (the configuration evolution) for these two extreme cases are illustrated in figure 12*a*,*b*, respectively, together with the limiting critical indentation displacement and the limiting detachment distance bounding the behaviours of the intermediate indenter size shown in figure 12*c*. Specifically, figure 12*c*(iii) depicts the relationship between the normalized critical snapping displacement, w_s/R, and the relative indenter size, r/R, as shown by the solid lines, in which circles represent the cases with varying finite indenter radius. It is clearly shown that those two extreme cases cover the upper and lower bounds of the cases with finite indenter radius. Similarly, figure 12*c*(ii) shows the dependence of the midpoint distance, $\Delta H/R$, on the normalized indenter size, r/R, and again, the upper and lower bounds for the cases with finite indenter radius are covered.

5. Conclusion

In this paper, we investigate the contact-induced snap-through of an axisymmetric shell by employing a recently developed order-reduced one-dimensional discrete model. Our numerical framework is comprised of two components: (i) DDG-based method for the geometrically nonlinear description of a rotational symmetric thin shell and (ii) incremental potential-based formulation for the boundary nonlinear contact between a rigid indenter and a flexible shell. The nonlinear system is later numerically solved by using the classical Newton–Raphson method. With the help of our computationally efficient and numerically robust framework, we find that the behaviour of thin spherical shells with different thicknesses and meridional angles can be categorized into three groups: (i) monotonous, (ii) monostable, and (iii) bistable. These different behaviours can apparently be uniquely characterized by the ratio of the shell's stretching energy to its bending energy, and by a simple scaling law that sets the boundaries between different regimes. Furthermore, we demonstrate that even a seemingly simple problem like spherical shells under a rigid spherical indenter loading exhibits interesting phenomena. Our results show that the tip of the indenter is not always in contact with the pole of the shell during deformation, but will create a gap when the radius of the rigid indenter is larger than the threshold value, leading to decreasing critical everting displacement. We also discover that, for bistable spherical shells, their deformed shape at the point of snapping is universal, independent of the type of loading (e.g. point load or rigid indenters of different radii), and can be captured by simple geometric analysis. We hope our findings can support the mechanical analysis and design of shell structures in both natural environments and engineered systems, e.g. cell fusion, tube necking and submarine collapsing.

Data accessibility. The code for the main paper are available at [48].

The code for the full three-dimensional FEM simulations is in Appendix B, which is modified from another open source [49].

Declaration of AI use. We have not used AI-assisted technologies in creating this article.

Authors' contributions. W.H.: conceptualization, formal analysis, investigation, methodology, software, validation, visualization, writing—original draft; Z.L.: data curation, software, visualization, writing—review and editing; M.L.: conceptualization, formal analysis, funding acquisition, investigation, methodology, project administration, resources, supervision, writing—review and editing; K.J.H.: conceptualization, formal analysis, funding acquisition, project administration, resources, supervision, writing—review and editing.

All authors gave final approval for publication and agreed to be held accountable for the work performed therein.

Conflict of interest declaration. We declare we have no competing interests.

Funding. W.H. acknowledges the financial support from the startup funding from Newcastle University. M.L. acknowledges the startup funding from the University of Birmingham. K.J.H. acknowledges the financial support from Nanyang Technological University, Singapore (Grant M4082428), and the Ministry of Education, Singapore, under its Academic Research Fund Tier 3 (Grant MOE-MOET32022-0002).

Acknowledgements. We are grateful to Dominic Vella, Yuzhen Chen and Tianzhen Liu for their valuable discussions, and to Peifei Xu for assistance with the FEM simulations.

Appendix A

The FEM simulation is applied to investigate the deformation mechanisms of spherical shells under the indentation of rigid spherical indenter of different sizes. The obtained results are compared with the discrete numerical model to verify the accuracy of the presented model. The FEM model is the same as the model presented in Huang *et al.* [43]. The definitions for the geometry and boundary conditions are identical to the main text. In addition, the models with a frictionless surface ($\mu_f = 0.0$) and a roughened surface ($\mu_f = 0.8$) are simulated to examine the effect of friction. We found no difference between the frictional and frictionless cases.

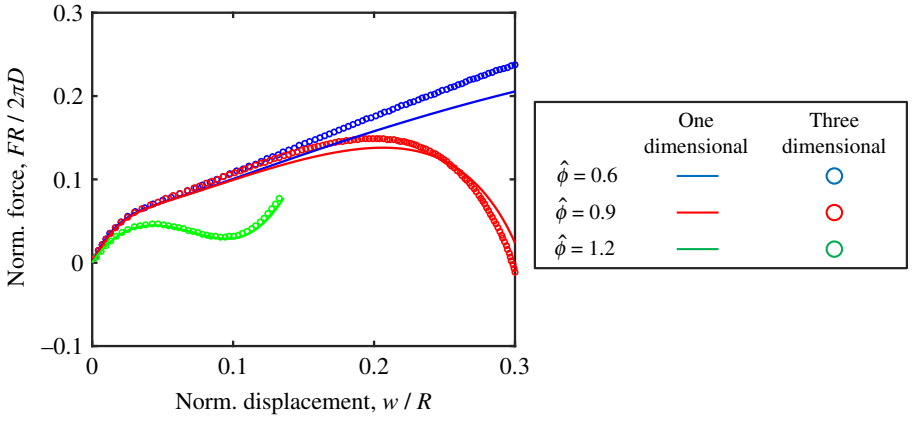

Figure 13. Force–displacement relationship for shells with different sizes. The curves are from the one-dimensional model, and the symbols are from the three-dimensional simulation.

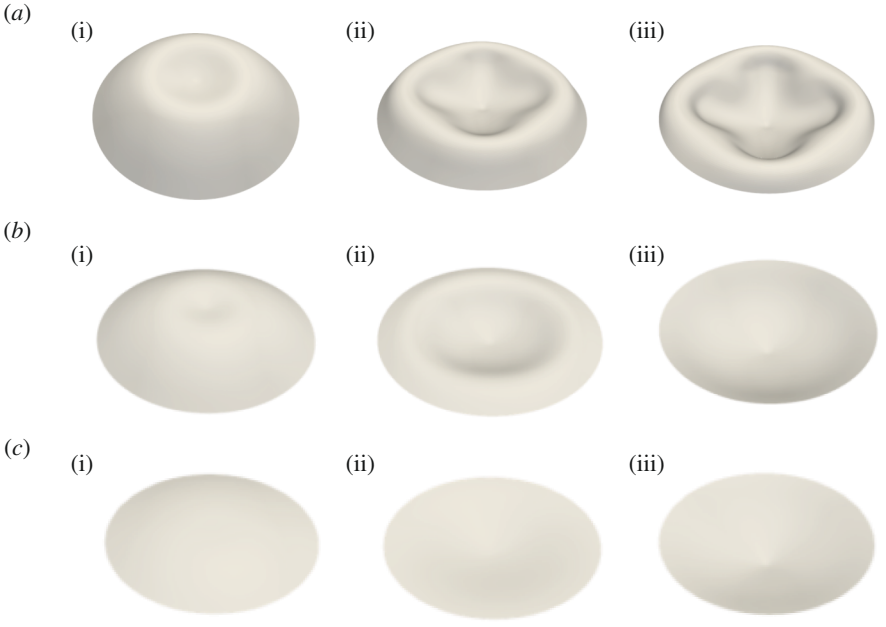

Figure 14. The configuration evolution of spherical shell cap under pole indention in three-dimensional FEM simulation. (*a*) $\hat{\phi} = 0.6$. (*b*) $\hat{\phi} = 0.9$. (*c*) $\hat{\phi} = 1.2$. The thickness is $h/R = 0.02$.

Appendix B

In this appendix, we use full three-dimensional FEM simulations to validate our one-dimensional symmetric simulation results [46]. Three-dimensional FEM simulations allow possible non-axisymmetric deformation for axisymmetric shells under a point force at the pole. Figure 13 shows the normalized force, $FR/2\pi D$, as a function of normalized pole displacement, w/R, for a shell with different configurations, $\hat{\phi} \in \{0.6, 0.9, 1.2\}$, and the thickness-to-radius ratio is fixed as $h/R = 0.02$. Good agreement is obtained for shallow shells, while deviations occur as the shell becomes deeper. The configuration evolution obtained from the three-dimensional FEM simulations can be found in figure 14. Not surprisingly, the deformation mode for a shallow

shell is symmetric, while that for deeper shells may become non-axisymmetric, e.g. $\hat{\phi} = 0.6$. In three-dimensional FEM, we also observed that the final results were not sensitive to the initial imperfection of the shell, mainly due to the sliding boundary condition at the bottom, which is consistent with the existing study [50]. In the current study, we focus on shallow shells thus our one-dimensional model (e.g. $\hat{\phi} > 0.9$) is valid in this regime.

References

1. Nasir AM. 2002 Axisymmetric shell structures for multi-use (PhD thesis). Brisbane, Australia: Queensland University of Technology.
2. Nelson R. 1978 Investigation of shell and axisymmetric shell structures (PhD Thesis). London, UK: City University London.
3. Taffetani M, Jiang X, Holmes DP, Vella D. 2018 Static bistability of spherical caps. *Proc. R. Soc. A* **474**, 20170910. (doi:10.1098/rspa.2017.0910)
4. Reis PM. 2015 A perspective on the revival of structural (in)stability with novel opportunities for function: from buckliphobia to buckliphilia. *J. Appl. Mech.* **82**, 111001. (doi:10.1115/1.4031456)
5. Bertoldi K, Vitelli V, Christensen J, van Hecke M. 2017 Flexible mechanical metamaterials. *Nat. Rev. Mater.* **2**, 1–11. (doi:10.1038/natrevmats.2017.66)
6. Vasios N, Deng B, Gorissen B, Bertoldi K. 2021 Universally bistable shells with nonzero Gaussian curvature for two-way transition waves. *Nat. Commun.* **12**, 695. (doi:10.1038/s41467-020-20698-9)
7. Liu M, Domino L, Dupont de Dinechin I, Taffetani M, Vella D. 2023 Snap-induced morphing: from a single bistable shell to the origin of shape bifurcation in interacting shells. *J. Mech. Phys. Solids* **170**, 105116. (doi:10.1016/j.jmps.2022.105116)
8. Yang X, Zhou Y, Zhao H, Huang W, Wang Y, Hsia KJ, Liu M. 2023 Morphing matter: from mechanical principles to robotic applications. *Soft Sci.* **3**, 38. (doi:10.20517/ss.2023.42)
9. Shim J, Perdigou C, Chen ER, Bertoldi K, Reis PM. 2012 Buckling-induced encapsulation of structured elastic shells under pressure. *Proc. Natl Acad. Sci. USA* **109**, 5978–5983. (doi:10.1073/pnas.1115674109)
10. Chen Y, Liu T, Jin L. 2022 Spatiotemporally programmable surfaces via viscoelastic shell snapping. *Adv. Intell. Syst.* **4**, 2100270. (doi:10.1002/aisy.202100270)
11. Forterre Y, Skotheim JM, Dumais J, Mahadevan L. 2005 How the Venus flytrap snaps. *Nature* **433**, 421–425. (doi:10.1038/nature03185)
12. Gorissen B, Melancon D, Vasios N, Torbati M, Bertoldi K. 2020 Inflatable soft jumper inspired by shell snapping. *Sci. Robot.* **5**, eabb1967. (doi:10.1126/scirobotics.abb1967)
13. Virot E, Kreilos T, Schneider TM, Rubinstein SM. 2017 Stability landscape of shell buckling. *Phys. Rev. Lett.* **119**, 224101. (doi:10.1103/PhysRevLett.119.224101)
14. Liu T, Chen Y, Liu L, Liu Y, Leng J, Jin L. 2021 Effect of imperfections on pseudo-bistability of viscoelastic domes. *Extreme Mech. Lett.* **49**, 101477. (doi:10.1016/j.eml.2021.101477)
15. Brinkmeyer A, Santer M, Pirrera A, Weaver PM. 2012 Pseudo-bistable self-actuated domes for morphing applications. *Int. J. Solids Struct.* **49**, 1077–1087. (doi:10.1016/j.ijsolstr.2012.01.007)
16. Nasto A, Ajdari A, Lazarus A, Vaziri A, Reis PM. 2013 Localization of deformation in thin shells under indentation. *Soft Matter* **9**, 6796. (doi:10.1039/c3sm50279a)
17. Yan D, Pezzulla M, Cruveiller L, Abbasi A, Reis PM. 2021 Magneto-active elastic shells with tunable buckling strength. *Nat. Commun.* **12**, 2831. (doi:10.1038/s41467-021-22776-y)
18. Abbasi A, Chen T, Aymon BFG, Reis PM. 2024 Leveraging the Snap Buckling of Bistable Magnetic Shells to Design a Refreshable Braille Dot. *Adv. Mater. Technol.* **9**, 2301344. (doi:10.1002/admt.202301344)
19. Kim Y, van den Berg J, Crosby AJ. 2021 Autonomous snapping and jumping polymer gels. *Nat. Mater.* **20**, 1695–1701. (doi:10.1038/s41563-020-00909-w)

20. Abdullah AM, Braun PV, Hsia KJ. 2016 Programmable shape transformation of elastic spherical domes. *Soft Matter* **12**, 6184–6195. (doi:10.1039/c6sm00532b)
21. Zhang Z, Pusateri S, Xie B, Hu N. 2020 Tunable energy trapping through contact-induced snap-through buckling in strips with programmable imperfections. *Extreme Mech. Lett.* **37**, 100732. (doi:10.1016/j.eml.2020.100732)
22. Qiao C, Liu L, Pasini D. 2021 Bi-shell valve for fast actuation of soft pneumatic actuators via shell snapping interaction. *Adv. Sci.* **8**, e2100445. (doi:10.1002/advs.202100445)
23. Madhukar A, Perlitz D, Grigola M, Gai D, Jimmy Hsia K. 2014 Bistable characteristics of thick-walled axisymmetric domes. *Int. J. Solids Struct.* **51**, 2590–2597. (doi:10.1016/j.ijsolstr.2014.03.022)
24. Hutchinson JW. 2016 Buckling of spherical shells revisited. *Proc. R. Soc. A* **472**, 20160577. (doi:10.1098/rspa.2016.0577)
25. Hutchinson JW, Thompson JMT. 2017 Nonlinear buckling interaction for spherical shells subject to pressure and probing forces. *J. Appl. Mech.* **84**, 6. (doi:10.1115/1.4036355)
26. Holmes DP, Lee JH, Park HS, Pezzulla M. 2020 Nonlinear buckling behavior of a complete spherical shell under uniform external pressure and homogenous natural curvature. *Phys. Rev. E* **102**, 023003. (doi:10.1103/PhysRevE.102.023003)
27. Carlson R, Sendelbeck R, Hoff N. 1967 Experimental studies of the buckling of complete spherical shells: the buckling behavior of electroformed spherical shells under uniform external pressure is examined in rigid and soft testing systems. *Exp. Mech.* **7**, 281–288. (doi:10.1007/BF02327133)
28. Yan D, Pezzulla M, Reis PM. 2020 Buckling of pressurized spherical shells containing a through-thickness defect. *J. Mech. Phys. Solids* **138**, 103923. (doi:10.1016/j.jmps.2020.103923)
29. Qiao C, Liu L, Pasini D. 2020 Elastic thin shells with large axisymmetric imperfection: from bifurcation to snap-through buckling. *J. Mech. Phys. Solids* **141**, 103959. (doi:10.1016/j.jmps.2020.103959)
30. Vinogradov AM, Glockner PG. 1980 Buckling of spherical viscoelastic shells. *J. Struct. Div.* **106**, 59–67. (doi:10.1061/JSDEAG.0005359)
31. Xirouchakis PC, Jones N. 1980 Axisymmetric and bifurcation creep buckling of externally pressurised spherical shells. *Int. J. Solids Struct.* **16**, 131–148. (doi:10.1016/0020-7683(80)90030-X)
32. Miyazaki N, Hagihara S. 2015 Creep buckling of shell structures. *Mech. Eng. Rev.* **2**, 14–00522(doi:10.1299/mer.14-00522)
33. Liu T, Chen Y, Hutchinson JW, Jin L. 2022 Buckling of viscoelastic spherical shells. *J. Mech. Phys. Solids* **169**, 105084. (doi:10.1016/j.jmps.2022.105084)
34. Sanders Jr, J. L. 1963 Nonlinear theories for thin shells. *Quart. Appl. Math.* **21**, 21–36. (doi:10.1090/qam/147023)
35. Cui XY, Wang G, Li GY. 2016 A nodal integration axisymmetric thin shell model using linear interpolation. *Appl. Math. Model.* **40**, 2720–2742. (doi:10.1016/j.apm.2015.09.077)
36. Pezzulla M, Reis PM. 2019 A weak form implementation of nonlinear axisymmetric shell equations with examples. *J. Appl. Mech.* **86**, 124502. (doi:10.1115/1.4044816)
37. Stein-Montalvo L, Holmes DP, Coupier G. 2021 Delayed buckling of spherical shells due to viscoelastic knockdown of the critical load. *Proc. R. Soc. A* **477**, 20210253. (doi:10.1098/rspa.2021.0253)
38. Poincloux S, Vallat C, Chen T, Sano TG, Reis PM. 2023 Indentation and stability of woven domes. *Extreme Mech. Lett.* **59**, 101968. (doi:10.1016/j.eml.2023.101968)
39. Bergou M, Wardetzky M, Robinson S, Audoly B, Grinspun E. 2008 Discrete elastic rods. *ACM Trans. Graph.* **27**, 1–12. (doi:10.1145/1360612.1360662)
40. Huang W, Ma C, Chen Q, Qin L. 2022 A discrete differential geometry-based numerical framework for extensible ribbons. *Int. J. Solids Struct.* **248**, 111619. (doi:10.1016/j.ijsolstr.2022.111619)
41. Huang W, Qin L, Chen Q. 2022 Numerical exploration on snap buckling of a pre-stressed hemispherical gridshell. *J. Appl. Mech.* **89**, 011005. (doi:10.1115/1.4052289)
42. Jawed MK, Novelia A, O'Reilly OM. 2018 *A primer on the kinematics of discrete elastic rods*. Cham, Switzerland: Springer.

43. Huang W, Liu T, Liu Z, Xu P, Liu M, Chen Y, Hsia KJ. 2024 Discrete differential geometry-based model for nonlinear analysis of axisymmetric shells. *Int. J. Mech. Sci.* **283**, 109742. (doi:10.1016/j.ijmecsci.2024.109742)
44. Li M, Kaufman DM, Jiang C. 2021 Codimensional incremental potential contact. *ACM Trans. Graph.* **40**, 1–24. (doi:10.1145/3450626.3459767)
45. Huang W, Zhang Y, Yu T, Liu M. 2023 Bifurcations and stability analysis of elastic slender structures using static discrete elastic rods method. *J. Appl. Mech.* **90**, 9. (doi:10.1115/1.4062533)
46. Liu Z, McBride A, Ghosh A, Heltai L, Huang W, Yu T, Steinmann P, Saxena P. 2024 Computational instability analysis of inflated hyperelastic thin shells using subdivision surfaces. *Comput. Mech.* **73**, 257–276. (doi:10.1007/s00466-023-02366-z)
47. Li M, Ferguson Z, Schneider T, Langlois TR, Zorin D, Panozzo D, Jiang C, Kaufman DM. 2020 Incremental potential contact: intersection-and inversion-free, large-deformation dynamics. *ACM Trans. Graph.* **39**, 49. (doi:10.1145/3386569.3392425)
48. Huang W. 2024 Weicheng-Huang-mechanics/axisShellContactSnap: axix_shell_contact_snap (axis_shell_contact). Zenodo. (doi:10.5281/zenodo.13767850)
49. Bangerth W *et al.* 2024 Weicheng-Huang-mechanics/dealii_catmull_clark: 3d shell FEM simulation (3d_shell_simulation). Zenodo. (doi:10.5281/zenodo.13768995)
50. Chen Y, Liu T, Jin L. 2023 Pseudo-bistability of viscoelastic shells. *Philos. Trans. Roc. Soc. A* **381**, 20220026. (doi:10.1098/rsta.2022.0026)